

## Various antiphase domains in garnet-hosted omphacite in low-temperature eclogite: A FIB-TEM study on heterogeneous ordering processes

RYO FUKUSHIMA<sup>1,\*</sup>, TATSUKI TSUJIMORI<sup>1,2,†</sup>, AND NOBUYOSHI MIYAJIMA<sup>3,‡</sup>

<sup>1</sup>Graduate School of Science, Tohoku University, Sendai 980-8578, Japan

<sup>2</sup>Center for Northeast Asian Studies, Tohoku University, Sendai 980-8576, Japan

<sup>3</sup>Bayerisches Geoinstitut, Universität Bayreuth, 95440 Bayreuth, Germany

### ABSTRACT

Low-temperature omphacite has peculiar microstructures called “antiphase domains (APDs),” which can be formed via phase transition from disordered  $C2/c$  to ordered  $P2/n$  structure during cooling. Hence morphological analyses of the APDs of undeformed omphacite have a potential to unravel the temperature-time ( $T-t$ ) histories of the eclogite. We investigated five omphacite inclusions in a euhedral garnet porphyroblast obtained from low-temperature eclogite in Syros. The garnet (~6 mm in size) exhibits a distinct prograde chemical zoning and contains abundant mineral inclusions. Transmission electron microscope (TEM) observations of the focused ion beam (FIB) foils confirmed a heterogeneous distribution of equiaxed APDs (10–280 nm in diameter) and columnar APDs. Size distributions of the equiaxed APDs are characterized by kurtosis values of –0.45–3.91, which are larger than those in the matrix omphacite. The columnar APDs are subdivided into two types: dislocation-related (Type I) and inclusion–host interfacial (Type II). The presence of Type I APDs may suggest the inclusions were deformed prior to the host garnet growth. In contrast, Type II APDs, which are characterized by a bundle of stripe-like APDs (~40 nm in width) aligned perpendicular to the host garnet, imply the simultaneous growth of omphacite and garnet in a non-deformation state. The presence of these two contrasting APDs of omphacite inclusions in the single prograde-zoned garnet prevents a simple application of geospeedometry based on APD sizes. Nevertheless, our observations demonstrate that APDs are keys to understanding thermodynamic equilibrium states and the mineral growth kinetics during eclogitization.

**Keywords:** Omphacite, antiphase domain (APD), garnet, transmission electron microscopy (TEM), eclogite

### INTRODUCTION

Omphacite, clinopyroxene with a composition close to  $\text{Ca}_{0.5}\text{Na}_{0.5}[\text{Mg},\text{Fe}^{2+}]_{0.5}\text{Al}_{0.5}\text{Si}_2\text{O}_6$ , is one of the prominent minerals which, together with garnet, compose eclogite (cf. Tsujimori and Mattinson 2021). It occurs ubiquitously in a variety of high-pressure (HP) and ultrahigh-pressure (UHP) metamorphic rocks, typically in basaltic protoliths. Its parageneses and major-element compositions have been commonly used to characterize subducted oceanic-crusts in the HP–UHP metamorphic belts. Omphacite at high temperature has a cation-disordered structure with  $C2/c$  symmetry (e.g., Warner 1964; Clark et al. 1969). At temperatures recorded in blueschist and most orogenic eclogites, however, the difference in space-group symmetry between ordered  $P2/n$  omphacite and disordered  $C2/c$  diopside pyroxene allows miscibility regions between jadeitic pyroxene–omphacite ( $C2/c$ – $P2/n$ ) and augitic pyroxene–omphacite ( $C2/c$ – $P2/n$ ) (e.g., Matsumoto and Banno 1970; Yokoyama et al. 1976; Carpenter 1979a, 1980; Tsujimori 1997; Tsujimori and Liou 2004; Tsujimori et al. 2005; García-Casco et al. 2009; Takahashi et al. 2017).

Cation ordering in omphacite has been investigated in

numerous transmission electron microscopic (TEM) studies; the cation ordering forms characteristic bubble-like or column-like microstructures, called “antiphase domains (APDs).” If disordered omphacite is cooled down to some extent, multiple ordered phases nucleate and pin each other because of discrepancies in cation positions at their boundaries. These boundaries are commonly called “antiphase domain boundaries (APDBs)” and can be observed under TEM. It is considered that APDBs can be formed even if omphacite crystallizes in the  $P2/n$  stable field, as many researchers think that the nucleation of the disordered phase predates APDBs formation (e.g., Champness 1973; Carpenter 1978).

An averaged diameter of equiaxed APDs ( $\delta$ ) can be calculated with the following equation (Carpenter 1981):


$$\delta^8 = 8 \times 6 \times 10^{35} \exp(-75\,000/RT)t$$

where  $t$  is annealing time and  $T$  is temperature. This function involving  $t$  and  $T$  would allow for geothermometry and/or geospeedometry and lead to a deeper understanding of the kinetics of low- $T$  eclogitization of a subducting slab. However, the application of this equation to natural omphacites is not that simple because omphacite-bearing blueschists and orogenic eclogites have commonly undergone deformation and because the original APDBs would have been modified very easily (Van

\* E-mail: ryo.fukushima.p7@dc.tohoku.ac.jp. Orcid 0000-0003-2683-6757

† Orcid 0000-0001-9202-7312

‡ Orcid 0000-0002-6226-5675

 Open access: Article available to all readers online.

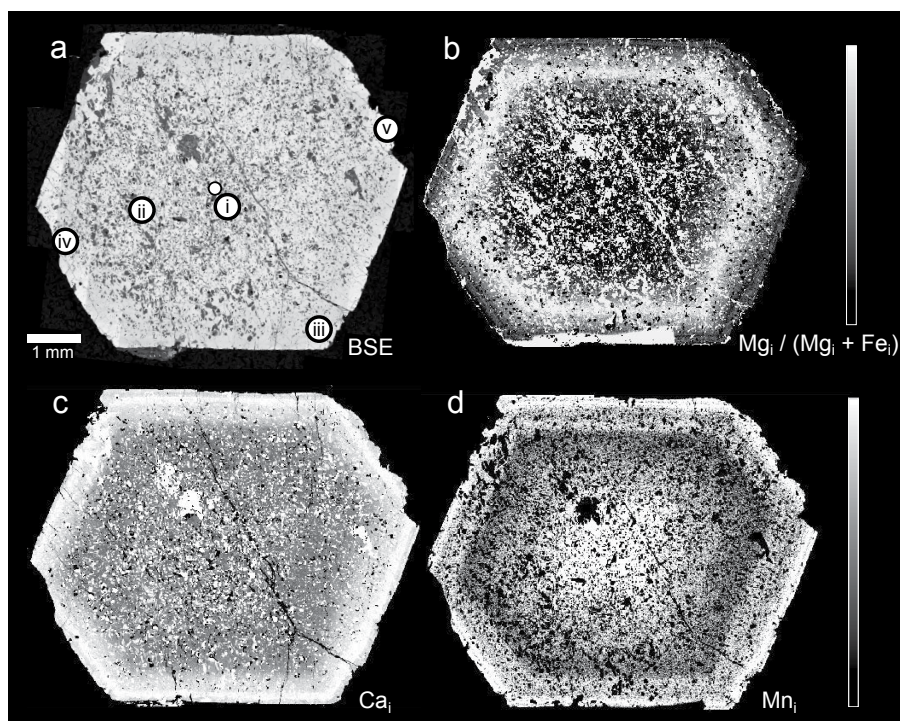
Roermund and Lardeaux 1991). Brenker et al. (2003) suggested a potential approach to exclude deformational modifications of original APDs. Specifically, they postulated that garnets could act as rigid capsules that prevent the dynamic recrystallization of omphacite inclusions. Nevertheless, no one has attempted to challenge the approach yet. Thus, in this study, we conducted a transmission electron microscopic (TEM) study combined with focused ion beam (FIB) technique on omphacite inclusions within a prograde-zoned garnet. The aim of our reconnaissance is to contribute to the understanding of the growth kinetics of omphacite inclusions within garnet porphyroblasts, as well as the low-*T* eclogitization of a subducting slab.

### SAMPLE DESCRIPTION

We examined a euhedral garnet porphyroblast (~6 mm in size) extracted from a low-*T* eclogite of the Cycladic Blueschist Unit (CBU), Syros, Greece (Fig. 1). The garnet exhibits a rhombic dodecahedron shape with 12 crystallographic equivalent {110} planes.

Syros Island, which belongs to Cyclades Archipelago, is located at the center of the Aegean domain. The metamorphic sequence consists mainly of alternating marbles and HP schists. The CBU of Syros contains dismembered meta-ophiolite, whose protoliths were derived from hydrothermally altered oceanic crust (Seck et al. 1996). The Cyclades Archipelago is the deepest exhumed parts of the belt and its peak-pressure conditions were achieved at ~53–48 Ma (Lagos et al. 2007; Lister and Forster 2016; Tomaschek et al. 2003; Uunk et al. 2018). The peak metamorphic condition of the CBU on Syros was estimated as *T* ~500–560 °C and *P* ~2.2–2.4 GPa (Laurent et al. 2018), while Schumacher et al. (2008) suggested a lower condition at *T* ~500 °C and *P* ~1.5–1.6 GPa.

**FIGURE 1.** Images of the investigated garnet: (a) BSE image; (b) X-ray map of Mg/(Mg+Fe) (intensity ratio); (c) X-ray map of Ca; (d) X-ray map of Mn. The subscript *i* after each element symbol indicates that the image was obtained based solely on the signal intensity. Locations of omphacite thin foils are also shown: (i) 1C, (ii) 2M, (iii) 3R, (iv) 4R, and (v) 5R. The white circle in the BSE image indicates the location of the garnet core estimated based on its euhedral outline and major-element zoning patterns.



### ANALYTICAL PROCEDURES

#### SEM observation and EPMA X-ray mapping

To characterize the core-to-rim compositional zoning of the porphyroblastic garnet, we first cut the extracted garnet at nearly the center. Then, one of the center-cut garnets was mounted with epoxy resin and polished. The polished sample was observed using a JEOL JSM-7001F field emission-scanning electron microscope (FE-SEM) at Tohoku University. The backscattered electron (BSE) imaging was performed at an acceleration voltage of 15 kV and a beam current of 3 nA. We identified mineral inclusions using a Hitachi S-3400N scanning electron microprobe (SEM) equipped with an Oxford INCA X-act energy-dispersive X-ray (EDS) system at Tohoku University. The acceleration voltage and the beam current during the SEM-EDS observations were maintained at 15 kV and 1 nA, respectively. X-ray mapping (Mg, Ca, Fe, and Mn) of the mounted garnet was performed by a JEOL JXA-8200 electron microprobe analyzer at Bayerisches Geoinstitut (BGI), at an acceleration voltage of 15 kV and a probe current of 500 nA.

#### FIB fabrication of omphacite

A FIB technique was used to extract foils of the omphacite inclusions in the garnet, using a FEI Scios DualBeam system equipped with a gallium (Ga) ion-gun for sample fabrication at BGI. Fabrication of thin foils (~100 nm in thickness) was done for the five omphacite inclusions [1C (core), 2M (mantle), 3R, 4R, 5R (rim)] in the order from the core to the rim of the garnet; for comparison, one foil (MX) was also extracted from a matrix-forming omphacite from the same eclogite. Note that we define two boundaries: one between the core and the mantle at 30% of the total radius from the center of crystal, and the other between the mantle and the rim at 85% (Fig. 2). These boundaries, respectively, correspond to the portion where the Y concentration peaks and the portion marking the beginning of Y-Mn enrichments (Fukushima et al. 2021). The locations of each inclusion can therefore be expressed as ~14% (1C), ~48% (2M), ~90% (3R), ~95% (4R), and ~98% (5R). The locations and morphology of the inclusions are shown in Figures 1 and 3.

#### TEM observation

The thin foil specimens of the omphacite inclusions were observed using an FEI Titan G2 80-200 S/TEM system and Philips CM20FEG at BGI. The microstructures of the omphacite were studied under conventional bright-field and dark-field TEM imaging modes and selected-area electron diffraction. In addition, EDS X-ray mapping

of major elements by scanning transmission electron microscopy (STEM), operated at a 200 kV acceleration voltage, was performed using four silicon drift detector (SDD) detectors. The STEM-EDS maps were generated by scanning a focused beam with a diameter of about 0.2 nm and a dwell time of 16  $\mu$ s across the samples.

### Measurement of antiphase domain (APD) sizes

To measure APD sizes, we processed the acquired digital images using an approach of the Trainable Weka Segmentation (Arganda-Carreras et al. 2017) bundled in an image processing package Fiji (Schindelin et al. 2012), which is a modified version of the open source, Java-based image processing program ImageJ (Abramoff et al. 2004). This application enables us to divide an image with complicated patterns into two or more groups based on its color distribution. In each dark-field image, we chose certain areas where many distinct APDs were observed to binarize them. Here, the binarized image reflects the difference in brightness between the ordered and disordered domains. Then, we excluded APDs with abnormal shapes by setting a threshold of circularity ( $= 4\pi \times \text{area}/\text{circumference}^2$ ). We also excluded some of the noise by setting a minimum APD size. Finally, we calculated the diameters of the APDs based on their areas, under the assumption that all of the measured APDs are circles.

To evaluate the reliability of this measurement protocol, in addition to our specimens, we also measured equiaxed APD sizes in a previously reported matrix-forming omphacite. Specifically, we processed the dark-field image (a scanned image from the literature) of sample 97647 in Carpenter (1978) (Fig. 2a in the literature) to measure its APD sizes.

### MINERAL INCLUSIONS IN THE ZONED GARNET

The investigated garnet crystal (Fig. 1) contains abundant mineral inclusions (typically ~10–100  $\mu$ m in size), mainly

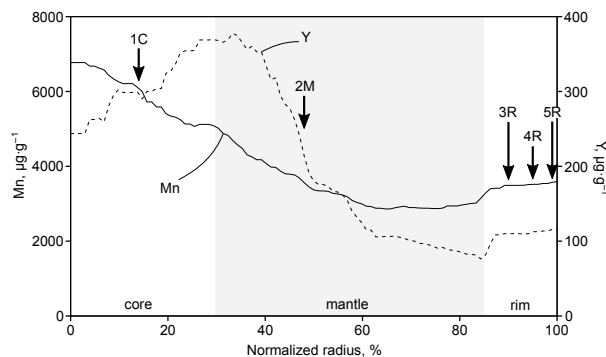


**FIGURE 2.** Representative line profiles of Mn (solid line) and Y (dashed line) in the investigated garnet. They represent kernel regression lines based on the measured data (Fukushima et al. 2021). Band widths are set to 27% for both. The region of the mantle (gray) is defined as 30–85% of the total radius. Approximate locations of the investigated omphacites are also shown.

of omphacite (~40–50 mol% jadeite) and clinozoisite [ $\text{Fe}^{3+}/(\text{Fe}^{3+}+\text{Al})$  atomic ratio = ~0.2]. Omphacite occurs as irregularly rounded anhedral crystals with curved interfaces. The garnet crystal also contains minor amounts of rutile, titanite, carbonates, apatite, chlorite, quartz, paragonite, albite, glaucophane, and zircon. Titanite tends to occur at the core. Chlorite and albite are found as secondary replacements of primary inclusions along micro cracks.

Major-element EPMA X-ray maps of the garnet (5–9 mol% pyrope; 61–67% almandine; 1–3% spessartine; 24–30% grossular) are shown in Figure 1. The maps exhibit a concentric zoning pattern, where  $\text{Mg}\# = \text{Mg}/(\text{Mg}+\text{Fe}^{2+})$  roughly increases rimward and Mn decreases from the core to the mantle. Subtle Mn enrichments are found at the rim.

### ANTIPHASE DOMAINS OF OMPHACITE

#### APD morphology and size distributions

TEM images of the omphacite inclusions are shown in Figures 4–6. Based on the morphology, the observed APDs are divided into two types: (1) equiaxed APDs and (2) columnar APDs. These two types frequently occur within a few micrometer-squared areas, and the boundaries among two types are not clear. The columnar APDs, with stripe-like shapes, are further subdivided into two types. Type I columnar APDs occur as extensions from dislocations. In contrast, Type II columnar APDs are found at garnet–omphacite interfaces and exhibit regular-alignment perpendicular to the interfaces. Note that, unless aligned periodically, dislocation-related columnar APDs attached perpendicularly to garnet–omphacite interfaces are classified as Type I columnar APDs.

We found equiaxed APDs in all of the FIB foils including omphacite in the eclogitic matrix, although they were less abundant in the 2M and 4R. Type I columnar APDs, most of which were highly curved, were also common in the omphacite inclusions. Type II columnar APDs were found only in 1C and 3R. Since the morphology of such columnar APDs is somewhat complicated, it is difficult to measure their widths. Therefore, we only measured equiaxed APD sizes here.

APD size variations are shown by histograms with the kernel density estimate in Figures 7 and 8. Measured data are presented in Online Material<sup>1</sup> Table OM1. Major modes are: ~40 nm (1C), ~30 nm (3R), ~20 nm (4R), ~60 nm (5R), ~60 nm (MX), and ~16 nm (sample 97647). Mean values are: 62 nm (1C), 67 nm

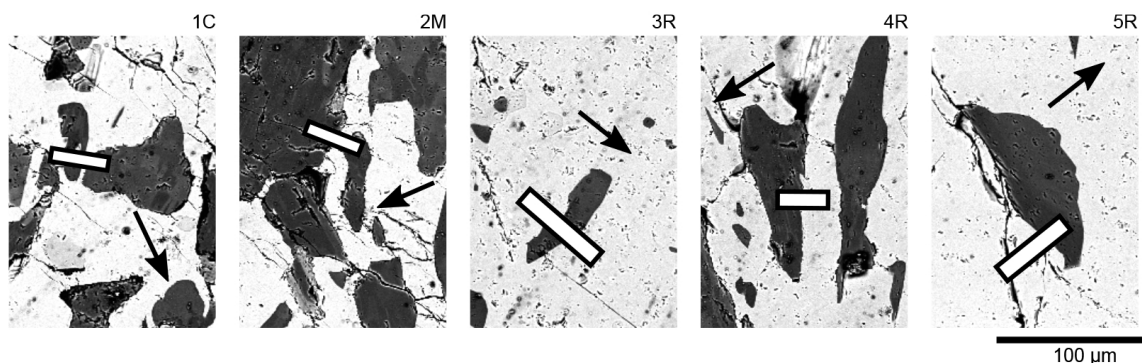


**FIGURE 3.** Locations of omphacite thin foils as indicated by the white rectangles. The black arrows indicate the directions to the center of the garnet core.

(3R), 25 nm (4R), 98 nm (5R), 88 nm (MX), and 31 nm (sample 97647). In addition, we calculated skewness and kurtosis values to characterize the distributions. We adopted the definitions of  $b_1$  (skewness) and  $b_2$  (kurtosis) as set forth in Joanes and Gill (1998). Skewness values are: 1.53 (1C), 0.64 (3R), 1.91 (4R), 0.77 (5R), 0.48 (MX), and 0.56 (sample 97647). Kurtosis values are: 3.14 (1C), -0.45 (3R), 3.91 (4R), 0.02 (5R), -0.85 (MX), and -0.65 (sample 97647). All of the APD size distributions are non-Gaussian and seem to be expressed by slightly multi-modal distributions. For each, the secondary or higher-order modes are larger than the major mode thereof, and the mean value is larger than the major mode by 5–38 nm. The mean equiaxed APD size of sample 97647 (Carpenter 1978) is consistent with the reported value of 20–50 nm. However, our reassessment also confirmed an abundance of APDs smaller than 20 nm.

### Peculiar features of individual APDs

**Omphacite extracted from the garnet core (1C).** 1C was extracted from the core of the garnet. Some regions of 1C (Fig. 4a) have both equiaxed APDs and Type II columnar APDs (width 20–130 nm, length ~130 nm). The widths of the Type II columnar APDs in 1C are not highly homogeneous (see Online Material<sup>1</sup> Table OM1 and Document OM1). The other regions, however, show abundant Type I columnar APDs (Fig. 4b). They seem to have highly interacted with dislocations in the omphacite. Although they are also roughly perpendicular to the garnet–omphacite interface, they are not periodic.

**Omphacite extracted from the mantle of the garnet (2M).** 2M was extracted from the mantle of the garnet. 2M (Fig. 5a) has mainly Type I columnar APDs and rare equiaxed APDs. Although these Type I columnar APDs are roughly perpendicular to the garnet–omphacite interface, they are not periodic.

**Omphacites extracted from the garnet rim (3R, 4R, and 5R).** 3R, 4R, and 5R were extracted from the rim of the garnet. 4R contains mainly Type I columnar APDs (Figs. 6a–6d), while 3R (Figs. 5b and 5c) and 5R (Fig. 6e) have mainly equiaxed APDs.

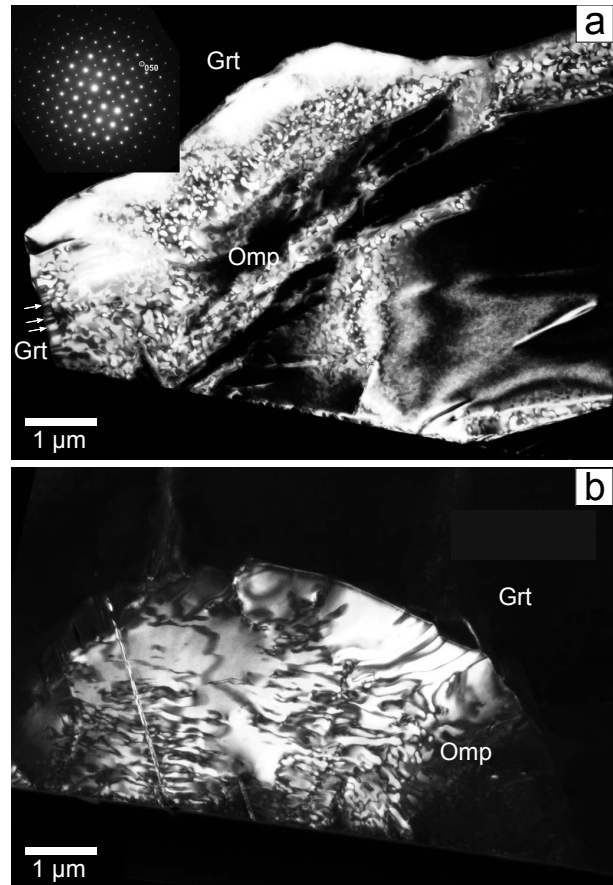


**FIGURE 4.** TEM images of 1C including garnet–omphacite interfaces: (a) dark-field image ( $g = 050$ ) of equiaxed/Type II columnar APDs and selected-area electron diffraction pattern ( $Z = [001]$ ) (inset); (b) dark-field image ( $g = 050$ ) of Type I columnar APDs. The white arrows in a indicate Type II columnar APDs. Grt = garnet, Omp = omphacite.

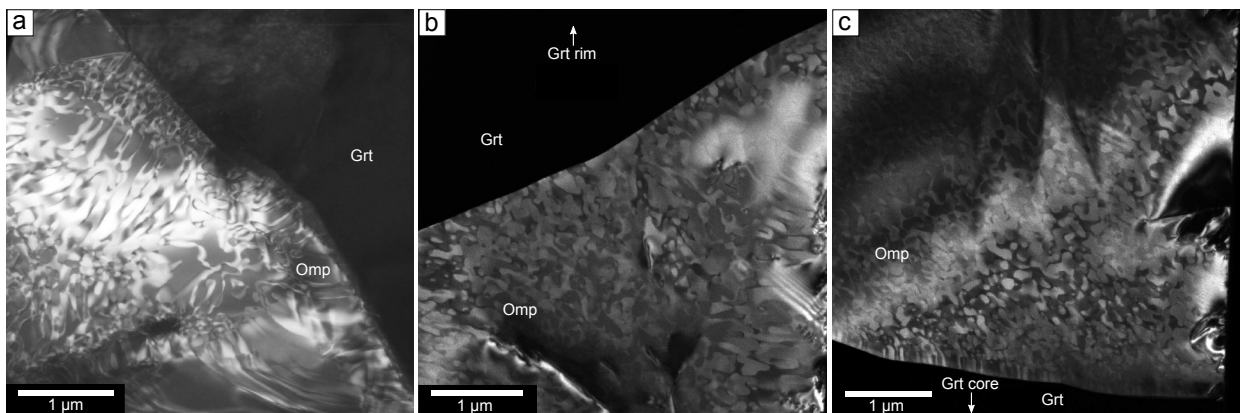
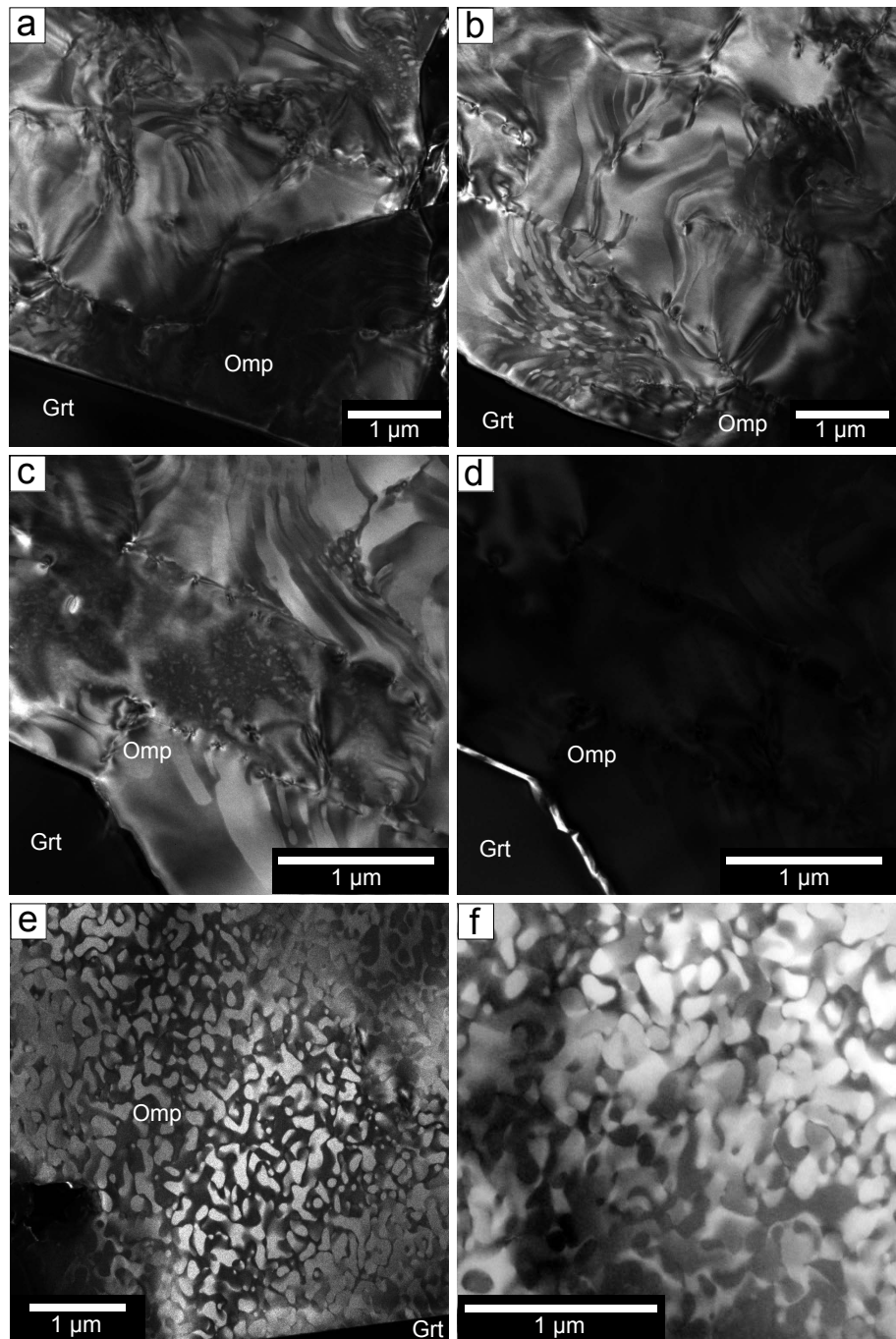


**FIGURE 5.** TEM images of 2M (a) and 3R (b and c): (a) dark-field image of 2M ( $g = \bar{1}40$ ) including a garnet–omphacite interface; (b) dark-field image of 3R ( $g = 050$ ) including a garnet–omphacite interface closer to the garnet rim; (c) dark-field image of 3R ( $g = 050$ ) including the other garnet–omphacite interface closer to the garnet core. At the bottom of (c), columnar APDs are aligned perpendicular to the garnet–omphacite interface (Type II columnar APDs).

**FIGURE 6.** TEM images of 4R (a–d), 5R (e), and MX (f): (a, b) dark-field images of 4R ( $g = 050$ ) including abundant Type I columnar APDs; (c) dark-field image of 4R ( $g = 050$ ) including a garnet–omphacite interface and equiaxed APDs; (d) bright-field image ( $g = 0\bar{5}0$ ) of the same area as (c); (e) dark-field image of 5R ( $g = 050$ ) including a garnet–omphacite boundary; (f) dark-field image of MX ( $g = 050$ ).



Equiaxed APDs were minor in 4R. The samples also showed differences with regards to APD shapes near the garnet–omphacite grain interfaces. In 4R, some Type I columnar APDs are attached perpendicularly to the garnet–omphacite interface (Fig. 6b), but the other regions never exhibit such textures (Fig. 6c). In the latter case, we observed fracture-like pores ( $\sim 50$  nm in width; Fig. 6d). In contrast, 5R does not contain Type I columnar APDs (Fig. 6e). 3R is similar to 5R in that both have abundant equiaxed APDs (Fig. 5b), but it is significantly different in the regions relatively close to the garnet core. Specifically, 3R encompasses Type II

columnar APDs (Fig. 5c), which are characterized by a bundle of elongated APDs aligned perpendicular to the garnet–omphacite interface. All of them are perpendicular to the interface and have a moderately homogenous width of  $38 \pm 11$  nm ( $n = 19$ ,  $1\sigma$ ) and length of  $\sim 130$  nm (see Online Material<sup>1</sup> Table OM1 and Document OM1). Although Type II columnar APDs were also observed in 1C, their widths are not highly homogeneous as in 3R. This peculiar texture was investigated by STEM-EDS X-ray mapping of Na, Ca, and Fe (Fig. 9). The Na- and Ca-distributions are homogenous throughout the specimen, while

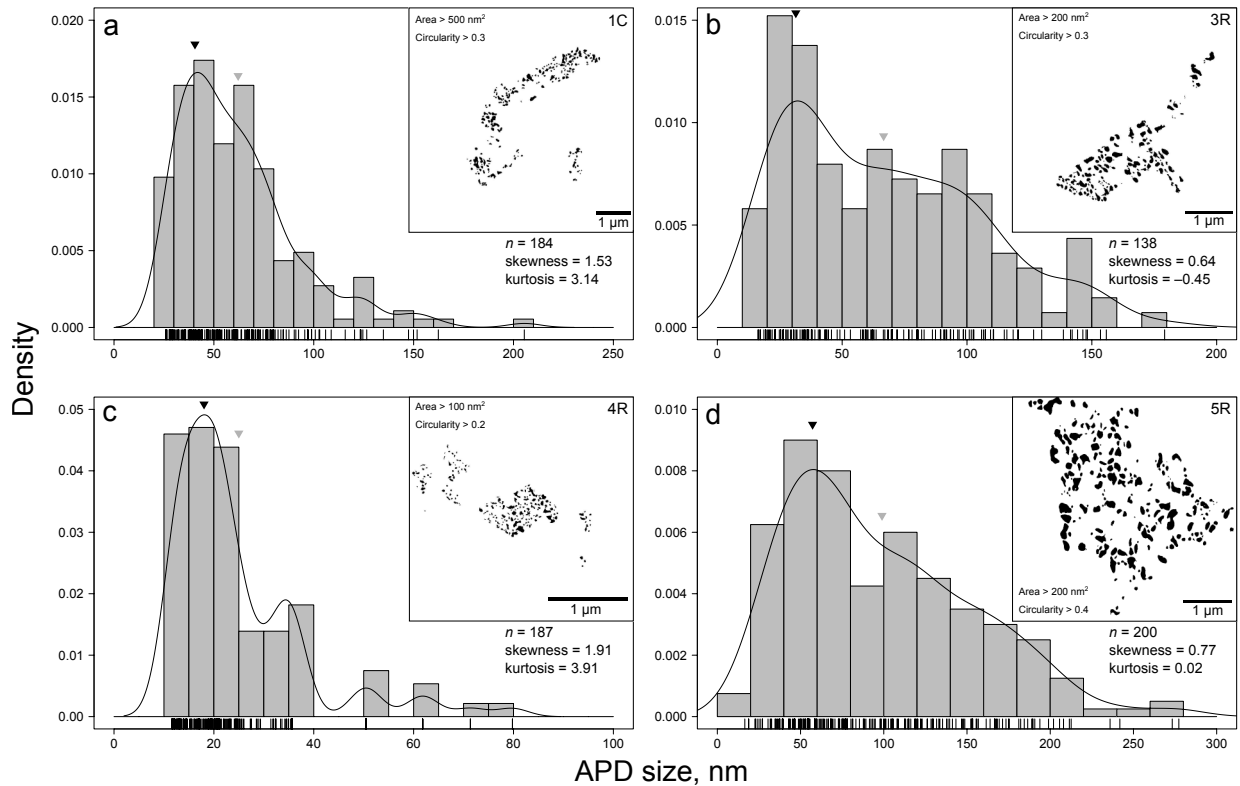


**FIGURE 7.** Histograms of measured APD sizes in (a) 1C, (b) 3R, (c) 4R, and (d) 5R. The insets show binarized dark-field images after the noise and highly distorted APDs are excluded. Results of the kernel density estimates are also shown. Band widths of the density estimates are: 8.303 nm (1C), 12.93 nm (3R), 3.214 nm (4R), and 17.07 nm (5R). For each diagram, the black and gray triangles indicate its mode and mean values, respectively.

the Fe concentration is slightly lower at the omphacite rim that has the Type II columnar APDs.

**Omphacite in the matrix (MX).** MX (Fig. 6f) has abundant equiaxed APDs as in 3R and 5R. No columnar APDs were observed.

## DISCUSSION

### Assessment of size distribution patterns of equiaxed APDs

**Implications from multi-modal size distributions.** Temperature dependence of APD coarsening in omphacite was proposed by Carpenter (1981). However, no appropriate method has existed for the quantification of apparent APD-size distribution. Since the multi-modal, non-Gaussian size distributions cannot be explained by a single nucleation event of the ordered phase, they must reflect complicated histories of the cation ordering in omphacite. Thus, assessment of the size distributions might enable us to discuss multiple nucleation events of the ordered phase. Although one should also consider some effects of deformation and impurity atoms at APDBs (Ling and Starke 1971; Rase and Mikkola 1975; Carpenter 1979b), the new measurement protocol gives us a key to predicting the cation ordering process at low temperature. In our observations, the mean equiaxed APD size in each of the specimens is larger than its major mode by 5–38 nm. Therefore, we cannot rule this out when discussing thermal events during the metamorphism. Moreover, this implies that mean equiaxed APD

sizes in omphacite, which are traditionally used for analyses of low-*T* metamorphic history, are not necessarily appropriate for geothermometry/geospeedometry.

**A comparison of garnet-hosted and matrix-forming omphacites.** Regarding equiaxed APD sizes, we could not confirm any significant difference between garnet-hosted and matrix-forming omphacite. However, we did find that the matrix-forming omphacites (MX and sample 97647) had lower skewness and kurtosis values than other samples. Notably, matrix-forming omphacites are likely to have lower kurtosis values; this implies that omphacites in an eclogitic matrix are likely to have wider ranges of APD sizes than omphacite inclusions in garnet. The relatively large APD-size variation in matrix omphacite would be attributed to strong syn- or post-metamorphic deformation effects, because the matrix should have been more subjected to deformation than omphacite inclusions enclosed in their rigid garnet. This tendency indicates that measuring APD sizes of “omphacite inclusions” may result in a better estimation of the metamorphic *T-t* history.

Considering these observations, we need to refine APD-size measurement protocol so that results can be obtained with less arbitrariness. Specifically, it is a crucial problem how we should deal with large and highly distorted APDs. For a better measurement, in essence, we have to interpret the kinetics of APD coarsening appropriately and set feasible thresholds to get results that make sense for the further discussion and implications.

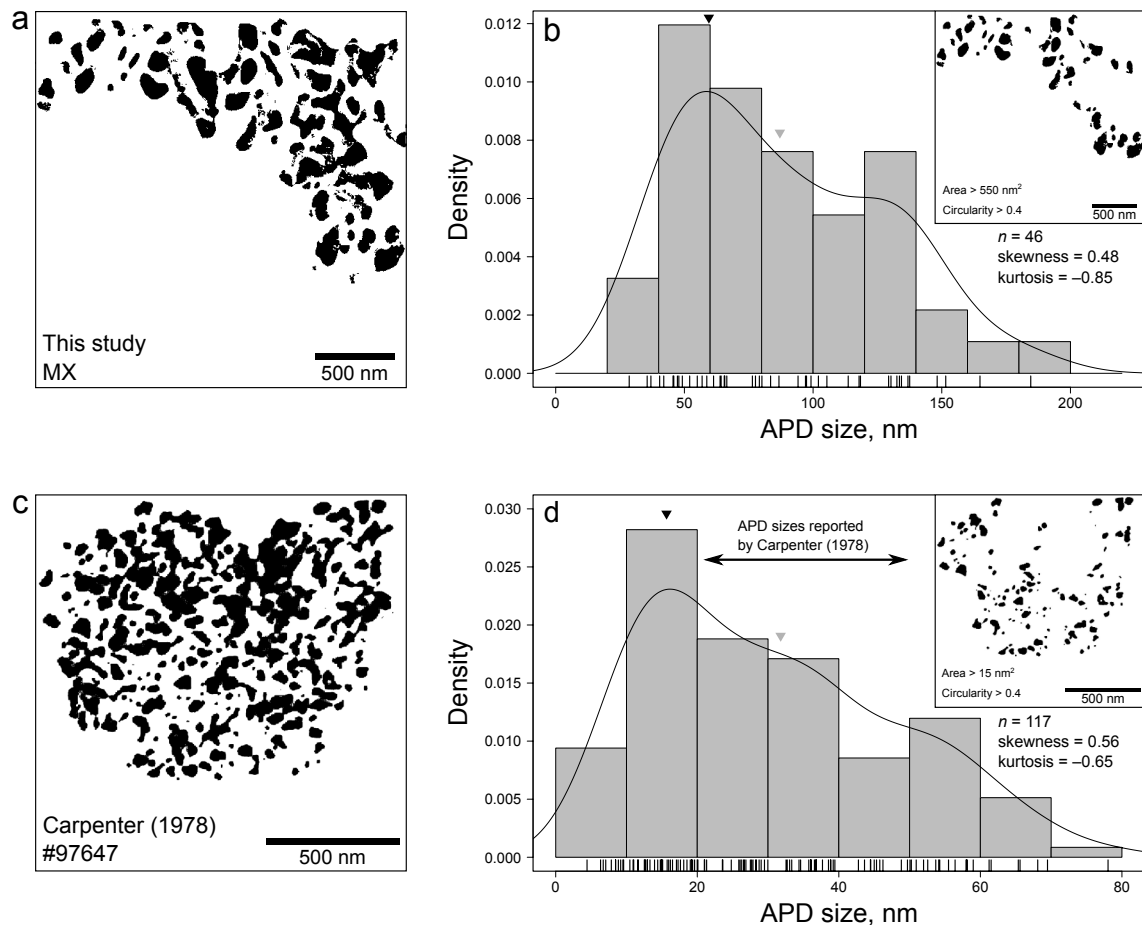


**FIGURE 8.** APD-size measurement results for matrix-forming omphacites [(a, b) MX; (c, d) sample 97647 in Carpenter (1978)]. Binarized images of dark-field TEM images are shown in (a and c), while histograms of measured APD sizes and the kernel density estimates are shown in (b and d). The insets in (b and d) show binarized images after noise and highly distorted APDs are excluded. Band widths of the density estimates are 16.54 nm (MX) and 6.031 nm (sample 97647). The black and gray triangles indicate the mode and mean values, respectively.

### The origins of columnar APDs

**Reassessment of the previously reported ordering mechanism.** We can explain the origins of columnar APDs on the basis of the previous idea that columnar APDs can be formed due to nucleation of the ordered phases at grain boundaries or low-angle subgrain boundaries (Lally et al. 1975; Carpenter 1979c). We can envisage a model in which cation ordering occurs at dislocations and/or garnet–omphacite interfaces and, consequently, the APDBs move from those locations.

As we described, however, Type II columnar APDs are less dominant. This is somewhat odd because all of the omphacite inclusions in the garnet have undergone the same metamorphic events, and also the surroundings of the rims of the omphacite inclusions would be similar. If the Type II columnar APDs can be formed merely by cation ordering initiating at garnet–omphacite interfaces due to the excess surface energy, such columnar APDs would be observed more frequently even in the other regions.

**The origin of Type II columnar APDs.** At the closer side of 3R to the garnet core, the widths of the Type II columnar APDs

are highly homogeneous and show a subtle discontinuity of Fe concentration (Fig. 9). This chemically discontinuous feature might indicate that the 3R rim with the Type II columnar APDs formed synchronously when the omphacite was included in the garnet. We interpret that Type II columnar APDs may commonly occur in syngenetic omphacite inclusions. Generally, omphacite can grow simultaneously with garnet in low-*T* eclogite (e.g., Konrad-Schmolke et al. 2008). Our *P-T* pseudosection modeling shows that omphacite with less Fe content is also likely to have grown with the garnet (see Online Material<sup>1</sup> Document OM2).

Then, the question arises: how can the Type II columnar APDs be formed in syngenetic omphacite? Considering the kinetics of the cation ordering, we propose two possible explanations. One is that the cation ordering occurred preferentially adjacent to preexisting ordered omphacite so that the total surface energy of the antiphase domain boundaries can be smaller. When omphacite grows slightly, the disordered phase first appears even though at a lower temperature than the ordering temperature of omphacite (e.g., Champness 1973; Carpenter 1978, 1980, 1981; Carpenter and Putnis 1985). If the

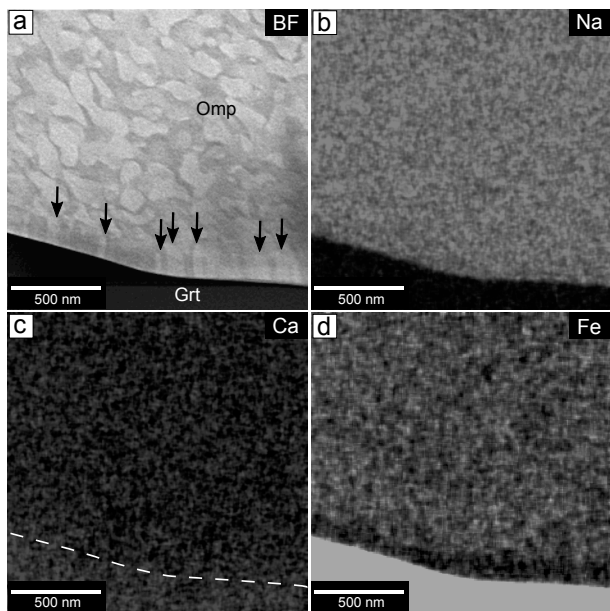


**FIGURE 9.** Scanning TEM images of the Type II columnar APDs in 3R: (a) image with a bright-field detector (BF); (b, c, d) X-ray maps of Na, Ca, and Fe, respectively. The black arrows in (a) indicate the Type II columnar APDs. The white dashed line in c depicts the garnet-omphacite interface.

preferential cation ordering occurred at the newly formed rim much faster than the omphacite growth, bundles of columnar APDs perpendicular to the garnet-omphacite interface are likely to be formed. It might be possible that the ordered phase grew almost epitaxially on the preexisting omphacite rim. In fact, this explanation is reasonable because columnar APDs in alloys can grow simultaneously with their crystallization from melt. For example, Mitsui et al. (1995) interpreted the origins of columnar APDs in Ni<sub>3</sub>Al and Cu<sub>3</sub>Pt alloys as the migration of grain boundaries of homogeneously ordered crystals. If this interpretation is correct, the widths of such Type II columnar APDs depend on initial equiaxed APD shapes at the pre-existing omphacite rim. Therefore, their widths do not necessarily depend only on the growth history of the omphacite rim. In this case, rimward changes of the columnar APD widths would be negligible because newly formed columnar APDs should have the same widths as the preexisting ones.

The alternative explanation is that the ordered phase nucleated in a periodic manner from garnet-omphacite interfaces after the

enclosed omphacite finished growing just as the metastable disordered phase. In this case, we cannot dismiss rimward changes of the Type II columnar APD widths. Since the ordered phase nucleates from the interfaces, wider APDs should be observed in closer regions to the omphacite rim. This width variation must reflect the metamorphic history after the omphacite was included in its host garnet.

The most crucial difference between these two possible scenarios is whether the columnar APD widths change rimward or not, but as shown in Figure 5c, this change is difficult to detect. Therefore, we cannot determine which explanation is correct without further information. To further our understanding, more observation is required than that documented in this study.

**Heterogeneous distributions of syngenetic omphacite inclusions.** If Type II columnar APDs are formed in syngenetic omphacite rims, the question that remains is why we seldom observe such omphacites. When pre-existing omphacites are enclosed in their host garnet, it seems that syn-metamorphic overgrowth does not necessarily occur in all of the omphacite rims. Thus, we discuss below this heterogeneous distribution of syngenetic omphacite rims in the single host garnet by considering its growth history (Fig. 10).

First, a garnet porphyroblast grows slightly to start to enclose an omphacite crystal. At that time, there must be a spatial gap between the garnet and the enclosed omphacite, as inferred from the presence of the fracture-like pores in 4R (e.g., Fig. 6d). Subsequently, if the spatial gap is filled with metamorphic fluids or Ca-Al silicates, the garnet grows slightly to fill the space. If the enclosed omphacite grows synchronously with the garnet, the spatial gap should be filled also by the growing omphacite. Note that we can regard the spatial gap as a small closed system wrapped by reaction products; in other words, the major elements for garnet-producing reactions cannot dissipate far away from the spatial gap. Thus, the omphacite can grow more efficiently within the spatial gap than other places as the host garnet grows slightly. Under this assumption, we can postulate a hypothesis that the heterogeneous distribution of syngenetic

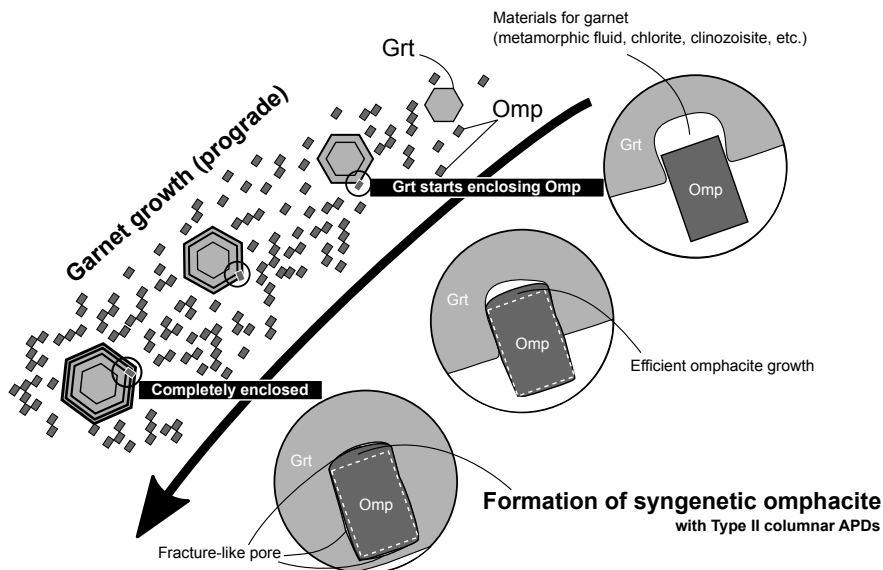


**FIGURE 10.** Schematic diagram illustrating our hypothesis to explain the heterogeneous distribution of syngenetic omphacites in a single host garnet.



omphacite rims is attributed to the heterogeneous presence of spatial gaps between the garnet and its omphacite inclusions. If this hypothesis is true, based on the most striking feature that 3R has Type II columnar APDs only on the side closer to the garnet core, we can assume that such small spatial gaps are likely to appear at the closer area to the garnet core. Moreover, this hypothesis might be reasonable because omphacite rims, grown in the spatial gap, are likely to be protected by the garnet from deformation disturbances.

## IMPLICATIONS

### New constraints on the growth kinetics of garnet-hosted omphacite

Our new finding of syngenetic omphacite with columnar APDs is highly valuable because it would allow us to study the kinetics of the cation ordering in omphacite. Although it is known that nucleation of the disordered phase predates the cation ordering, the kinetics of this process is unclear. Our observation of the periodic columnar APDs is a snapshot of growing omphacite with the cation ordering. Considering  $P$ - $T$ - $t$  information obtained on the basis of geochronology and compositional zoning patterns of garnet, we might be able to understand the initiation of the cation ordering at low temperature.

It is noteworthy that omphacite rims with bundles of columnar APDs would have formed just as they were incorporated into garnet. Over the years, the origins of mineral inclusions, whether they are formed simultaneously with incorporation of them or are remnant fragments of the protolith, are of interest. In the case of sector-zoned garnet, the phenomena that quartz inclusions simultaneously grow with the garnet, can be observed (Andersen 1984). Crystallographic orientations of mineral inclusions to their host garnet have been characterized with electron backscatter diffraction to estimate their origins (e.g., Griffiths et al. 2016; Ferrero and Angel 2018). However, it remains difficult to know whether a given mineral inclusion was incorporated into its host garnet simultaneously with its growth. Our finding of the heterogeneous distribution of Type II columnar APDs should therefore be a significant contribution to discussing the origins of mineral inclusions. If omphacite with such APDs is a product of reactions producing garnet, analyses of the APD shapes might unravel the timing at which the omphacite was included in the host garnet.

### Pitfalls of the APD geospeedometry

Since prograde-zoned garnet itself has a potential to determine  $P$ - $T$ - $t$  information, we might be able to estimate the garnet growth rate or the timescale of eclogitization by simply applying APD geospeedometry to the omphacite inclusions. However, our FIB-TEM study denies a simple application, because APD-size variation highly reflects a difference in the timings of the nucleation processes of the omphacite. In fact, all of the garnet-rim foils (3R, 4R, and 5R) were extracted from the same garnet rim but their equiaxed APD sizes are extremely different. In addition, the presence of Type I columnar APDs may suggest omphacite generally underwent deformation before being enclosed by garnet. To establish more sophisticated geospeedometry based on omphacite APDs, it is critical to focus on omphacite which grew synchronously with the host garnet. In other words, under-

standing of the timing of omphacite incorporation into its host garnet might lead to a refinement of the APD geospeedometry.

Nevertheless, it is not easy to extract temperature/time information only from the Type II columnar APDs because rimward changes of their shapes are small. Therefore, future work should be directed toward analyzing more omphacite inclusions within a single prograde-zoned garnet, understanding the critical trends of columnar APD shapes, and modeling their growths. This is important not only for understanding the kinetics of the cation ordering in omphacite but also for unraveling the kinetics of low- $T$  eclogitization in subduction zones.

## ACKNOWLEDGMENTS

This research was supported by CNEAS at Tohoku University, BGI at the University of Bayreuth, and the University of Tokyo, and was funded in part by grants from the MEXT/JSPS KAKENHI JP18H01299/JP21H01174 to T.T. and the ERI JURP 2018-B-01/2021-B-01 to T.T. and R.F. The authors acknowledge the International Joint Graduate Program in Earth and Environmental Sciences (GP-EES) and the JSPS Japanese-German Graduate Externship. The Scios FIB and the Titan G2 TEM at BGI were financed by DFG Grant Nos. INST 91/315-1 FUGG and INST 91/251-1 FUGG, respectively. We appreciate the comments from two anonymous reviewers. We also thank Bradley De Gregorio for constructive editorial evaluation.

## REFERENCES CITED

- Abramoff, M.D., Magalhães, P.J., and Ram, S.J. (2004) Image processing with ImageJ. *Biophotonics International*, 11, 36–42.
- Andersen, T.B. (1984) Inclusion patterns in zoned garnets from Magerøy, north Norway. *Mineralogical Magazine*, 48, 21–26.
- Arganda-Carreras, I., Kaynig, V., Rueden, C., Eliceiri, K.W., Schindelin, J., Cardona, A., and Seung, H.S. (2017) Trainable Weka Segmentation: A machine learning tool for microscopy pixel classification. *Bioinformatics*, 33, 2424–2426.
- Brenker, F.E., Müller, W.F., and Brey, G.P. (2003) Variation of antiphase domain size in omphacite: A tool to determine the temperature–time history of eclogites revisited. *American Mineralogist*, 88, 1300–1311.
- Carpenter, M.A. (1978) Kinetic control of ordering and exsolution in omphacite. *Contributions to Mineralogy and Petrology*, 67, 17–24.
- (1979a) Omphacites from Greece, Turkey, and Guatemala: Composition limits of cation ordering. *American Mineralogist*, 64, 102–108.
- (1979b) Experimental coarsening of antiphase domains in a silicate mineral. *Science*, 206, 681–683.
- (1979c) Contrasting properties and behaviour of antiphase domains in pyroxenes. *Physics and Chemistry of Minerals*, 5, 119–131.
- (1980) Mechanism of exsolution in sodic pyroxene. *Contributions to Mineralogy and Petrology*, 71, 289–300.
- (1981) Omphacite microstructures as time-temperature indicators of blueschist- and eclogite-facies metamorphism. *Contributions to Mineralogy and Petrology*, 78, 441–451.
- Carpenter, M.A., and Putnis, A. (1985) Cation order and disorder during crystal growth: Some implications for natural mineral assemblages. In A.B. Thompson and D.C. Rubie, Eds., *Metamorphic Reactions*, 1–26. Springer.
- Champness, P.E. (1973) Speculation on an order-disorder transformation in omphacite. *American Mineralogist*, 58, 540–542.
- Clark, J.R., Appleman, D.E., and Papike, J.J. (1969) Crystal-chemical characterization of clinopyroxene based on eight new structure refinements. *Mineralogical Society of America Special Paper*, 2, 31–50.
- Dale, J., Holland, T., and Powell, R. (2000) Hornblende  $\pm$  garnet  $\pm$  plagioclase thermobarometry: a natural assemblage calibration of the thermodynamics of hornblende. *Contributions to Mineralogy and Petrology*, 140, 353–362.
- de Capitani, C., and Brown, T.H. (1987) The computation of chemical equilibrium in complex systems containing non-ideal solutions. *Geochimica et Cosmochimica Acta*, 51, 2639–2652.
- de Capitani, C., and Petrakakis, K. (2010) The computation of equilibrium assemblage diagrams with Theriak/Domino software. *American Mineralogist*, 95, 1006–1016.
- Ferrero, S., and Angel, R.J. (2018) Micropetrology: Are inclusions grains of truth? *Journal of Petrology*, 59, 1671–1700.
- Fukushima, R., Tsujimori, T., Aoki, S., and Aoki, K. (2021) Trace-element zoning patterns in porphyroblastic garnets in low- $T$  eclogites: Parameter optimization of the diffusion-limited REE-uptake model. *Island Arc*, 30, e12394.
- García-Casco, A., Vega, A.R., Párraga, J.C., Iturralde-Vinent, M.A., Lázaro, C., Quintero, I.B., Agramonte, Y.R., Kröner, A., Cambra, K.N., Millán, G., and others (2009) A new jadeiteite jade locality (Sierra del Convento, Cuba): First report and some petrological and archeological implications. *Contributions to Mineralogy and Petrology*, 158, 1–16.

- Griffiths, T.A., Habler, G., and Abart, R. (2016) Crystallographic orientation relationships in host–inclusion systems: new insights from large EBSD data sets. *American Mineralogist*, 101, 690–705.
- Holland, T., and Powell, R. (1996) Thermodynamics of order–disorder in minerals: II. Symmetric formalism applied to solid solutions. *American Mineralogist*, 81, 1425–1437.
- (1998) An internally consistent thermodynamic data set for phases of petrological interest. *Journal of Metamorphic Geology*, 16, 309–343.
- (2003) Activity–composition relations for phases in petrological calculations: an asymmetric multicomponent formulation. *Contributions to Mineralogy and Petrology*, 145, 492–501.
- Holland, T., Baker, J., and Powell, R. (1998) Mixing properties and activity–composition relationships of chlorites in the system  $\text{MgO-FeO-Al}_2\text{O}_3\text{-SiO}_2\text{-H}_2\text{O}$ . *European Journal of Mineralogy*, 10, 395–406.
- Joanes, D.N., and Gill, C.A. (1998) Comparing measures of sample skewness and kurtosis. *The Statistician*, 47, 183–189.
- Keller, L.M., de Capitani, C., and Abart, R. (2005) A quaternary solution model for white micas based on natural coexisting phengite–paragonite pairs. *Journal of Petrology*, 46, 2129–2144.
- Konrad-Schmolke, M., O'Brien, P.J., de Capitani, C., and Carswell, D.A. (2008) Garnet growth at high- and ultra-high pressure conditions and the effect of element fractionation on mineral modes and composition. *Lithos*, 103, 309–332.
- Lagos, M., Scherer, E.E., Tomaschek, F., Munker, C., Keiter, M., Berndt, J., and Ballhaus, C. (2007) High precision Lu–Hf geochronology of Eocene eclogite–facies rocks from Syros, Cyclades, Greece. *Chemical Geology*, 243, 16–35.
- Lally, J.S., Heuer, A.H., Nord, G.L. Jr., and Christie, J.M. (1975) Subsolidus reactions in lunar pyroxenes: An electron petrographic study. *Contributions to Mineralogy and Petrology*, 51, 263–281.
- Laurent, V., Lanari, P., Nair, I., Augier, R., Lahfid, A., and Jolivet, L. (2018) Exhumation of eclogite and blueschist (Cyclades, Greece): Pressure–temperature evolution determined by thermobarometry and garnet equilibrium modeling. *Journal of Metamorphic Geology*, 36, 769–798.
- Ling, F.W., and Starke, E.A. Jr. (1971) The development of long-range order and the resulting strengthening effects in  $\text{Ni}_3\text{Mo}$ . *Acta Metallurgica*, 19, 759–768.
- Lister, G.S., and Forster, M.A. (2016) White mica  $^{40}\text{Ar}/^{39}\text{Ar}$  age spectra and the timing of multiple episodes of high-P metamorphic mineral growth in the Cycladic eclogite–blueschist belt, Syros, Aegean Sea, Greece. *Journal of Metamorphic Geology*, 34, 401–421.
- Matsumoto, T., and Banno, S. (1970) A natural pyroxene with space group  $\text{C}_{2h}^3 = \text{P}2/n$ . *Proceedings of the Japan Academy*, 46, 173–175.
- Mitsui, K., Suzuki, T., and Mishima, Y. (1995) Anti-phase domain morphology and its formation process in melt-quenched  $\text{Ni}_3\text{Al}$ . *Intermetallics*, 3, 161–166.
- Rase, C.L., and Mikkola, D.E. (1975) Effect of excess Au on antiphase domain growth in  $\text{Cu}_3\text{Au}$ . *Metallurgical and Materials Transactions A*, 6, 2267–2271.
- Schindelin, J., Arganda-Carreras, I., Frise, E., Kaynig, V., Longair, M., Pietzsch, T., Preibisch, S., Rueden, C., Saalfeld, S., Schmid, B., and others (2012) Fiji: An open-source platform for biological-image analysis. *Nature Methods*, 9, 676–682.
- Schumacher, J.C., Brady, J.B., Cheney, J.T., and Tonnsen, R.R. (2008) Glaucophane-bearing marbles on Syros, Greece. *Journal of Petrology*, 49, 1667–1686.
- Seck, H.A., Kötze, J., Okrusch, M., Seidel, E., and Stosch, H.G. (1996) Geochemistry of a meta-ophiolite suite: an association of metagabbros, eclogites and glaucophanites on the island of Syros, Greece. *European Journal of Mineralogy*, 8, 607–623.
- Takahashi, N., Tsujimori, T., Kayama, M., and Nishido, H. (2017) Cathodoluminescence petrography of P-type jadeites from the New Idria serpentinite body, California. *Journal of Mineralogical and Petrological Sciences*, 112, 291–299.
- Tomaschek, F., Kennedy, A.K., Villa, L.M., Lagos, M., and Ballhaus, C. (2003) Zircon from Syros, Cyclades, Greece – Recrystallization and mobilization of zircon during high-pressure metamorphism. *Journal of Petrology*, 44, 1977–2002.
- Trotet, F., Vidal, O., and Jolivet, L. (2001) Exhumation of Syros and Sifnos metamorphic rocks (Cyclades, Greece). New constraints on the *PT* paths. *European Journal of Mineralogy*, 13, 901–920.
- Tsujimori, T. (1997) Omphacite–diopside vein in an omphacite block from the Osayama serpentinite melange, Sangun–Renge metamorphic belt, southwestern Japan. *Mineralogical Magazine*, 61, 845–852.
- Tsujimori, T., and Liou, J.G. (2004) Coexisting chromian omphacite and diopside in tremolite schist from the Chugoku Mountains, SW Japan: The effect of Cr on the omphacite–diopside immiscibility gap. *American Mineralogist*, 89, 7–14.
- Tsujimori, T., and Mattinson, C. (2021) Eclogites in different tectonic settings. In S. Elias and D. Alderton, Ed., *Encyclopedia of Geology* (2nd ed.), 561–568. Academic Press.
- Tsujimori, T., Liou, J.G., and Coleman, R.G. (2005) Coexisting retrograde jadeite and omphacite in a jadeite-bearing lawsonite eclogite from the Motagua Fault Zone, Guatemala. *American Mineralogist*, 90, 836–842.
- Uunk, B., Brouwer, F., ter Voorde, M., and Wijbrans, J. (2018) Understanding phengite argon closure using single grain fusion age distributions in the Cycladic Blueschist Unit on Syros, Greece. *Earth and Planetary Science Letters*, 484, 192–203.
- Van Roermund, H.L.M., and Lardeaux, J.M. (1991) Modification of antiphase domain sizes in omphacite by dislocation glide and creep mechanisms and its petrological consequences. *Mineralogical Magazine*, 55, 397–407.
- Warner, J. (1964) X-ray crystallography of omphacite. *American Mineralogist*, 49, 1461–1467.
- Wei, C.J., Powell, R., and Zhang, L.F. (2003) Eclogites from the south Tianshan, NW China: petrological characteristic and calculated mineral equilibria in the  $\text{Na}_2\text{O-CaO-FeO-MgO-Al}_2\text{O}_3\text{-SiO}_2\text{-H}_2\text{O}$  system. *Journal of Metamorphic Geology*, 21, 163–179.
- White, R.W., Powell, R., and Phillips, G.N. (2003) A mineral equilibria study of the hydrothermal alteration in mafic greenschist facies rocks at Kalgoorlie, Western Australia. *Journal of Metamorphic Geology*, 21, 455–468.
- Yokoyama, K., Banno, S., and Matsumoto, T. (1976) Compositional range of *P2/n* omphacite from the eclogitic rocks of central Shikoku, Japan. *Mineralogical Magazine*, 40, 773–779.

MANUSCRIPT RECEIVED OCTOBER 18, 2020

MANUSCRIPT ACCEPTED NOVEMBER 16, 2020

MANUSCRIPT HANDLED BY BRADLEY DE GREGORIO

### Endnote:

<sup>1</sup>Deposit item AM-21-107784, Online Materials. Deposit items are free to all readers and found on the MSA website, via the specific issue's Table of Contents (go to [http://www.minsocam.org/MSA/AmMin/TOC/2021/Oct2021\\_data/Oct2021\\_data.html](http://www.minsocam.org/MSA/AmMin/TOC/2021/Oct2021_data/Oct2021_data.html)).